Sn-doped CeO_2 Nanorods as High-Performance Electrocatalysts for CO_2 Reduction to Formate

Shunlian Ning,[a] Zhiwei Guo,[a] Jigang Wang,[a] Shaobin Huang,[a] Shaowei Chen,*[b] and Xiongwu Kang*[a]

Electrochemical reduction of carbon dioxide to formate provides an effective way to solve the environmental problems caused by excessive carbon dioxide emissions and produce value-added products. Herein, we report the preparation of a Sn-doped CeO_2 catalyst, where oxygen vacancies are formed by thermal treatment in Ar/H_2 atmosphere, leading to enhanced carbon dioxide electroreduction to formate. The Faraday efficiency of formate production is found to reach 81.10%, with a geometric current density of 9.13 mA cm^{-2} at a potential of −1.10 V versus reversible hydrogen electrode. Density functional theory calculations show that the incorporation of tin into CeO_2 promotes electron transport, lowers the energy barrier to form formate through HCOO*, and increases the selectivity of formate. Results from this study highlight the importance of metal-doping in CeO_2 towards the selective reduction of CO_2 to formate.

1. Introduction

Extensive use of fossil fuels leads to the release of a large amount of CO_2, which poses a significant threat to global climate and environment.[1] Therefore, high-efficiency and low-cost technologies are urgently sought to reduce CO_2 in the atmosphere,[2] in which electrochemical CO_2 reduction reaction (CO_2RR) represents an effective strategy to convert carbon dioxide (CO_2) gas into value-added chemicals (e.g., CO, CH_4, C_2H_4, HCOOH, etc).[3] However, CO_2RR generally requires an excessive potential, as the Faraday efficiency (FE) is low and product selectivity is poor due to the competitive hydrogen evolution reaction (HER), resulting in a decrease of the carbon products.[4] For instance, and electroreduction of CO_2 to formate has been attracting a great deal of interest, as formate is a stable non-toxic liquid that has great market values in diverse applications, such as hydrogen carrier systems[5] and formate fuel cells.[6] Yet, this CO_2RR process involves multiple electron/proton transfer steps, and it is of fundamental significance to develop effective electrocatalysts to facilitate the reaction. Towards this end, a range of bimetallic and non-metal/metal-doped catalysts have been developed.[7]

Ceria is a well-known material for oxygen storage[8] with strong metal-support interactions,[9] but its performance is not ideal as a CO_2RR catalyst due to its poor electronic conductivity and competitive hydrogen evolution as electrocatalyst. A range of strategies have been adopted to improve the catalytic efficiency, where surface modification via metal doping represents an effective approach. For instance, Zheng and co-workers reported that CO_2 adsorption and reduction was enhanced with Cu-substituted CeO_2 due to the generation of multiple oxygen vacancies, and the best catalyst showed an FE of 58% for CH_4 at −1.80 V vs. RHE.[7b] Bao et al. argued that the Au-CeO_x interface enhanced CO_2 adsorption and stabilized key carboxyl intermediates (COOH*), leading to a high FE of 89.1% for CO production at −0.89 V vs. RHE.[7a] However, studies of the catalytic activity and mechanism of Sn-doped CeO_2 for CO_2RR have been scarce.[10] It has been shown that Pd,[11] Sn,[12] Bi,[13] and In[14] are effective in selective reduction of CO_2 to formate. Among these, tin (Sn) is a relatively inexpensive and environmentally friendly metal and has been attracting extensive interest as an excellent electrocatalyst for CO_2RR. For example, Qiao et al. prepared a Sn-doped copper alloy that selectively produced formate through the Sn sites.[15] This is mostly due to the excessively high potentials required for HER.[16]

Herein, we report the facile synthesis of the Sn-doped CeO_2 nanorods via a facile hydrothermal method. After thermal annealing in an Ar/H_2 atmosphere, the obtained catalyst showed a remarkable electrocatalytic activity for the production of formate from CO_2RR in a CO_2-saturated $NaHCO_3$ (0.1 mol L^{-1}) electrolyte, and the sample with a 10% mass of Sn shows the highest FE (81.10%) and current density of 9.13 mA cm^{-2} at −1.10 V vs. RHE. This high activity and selectivity are largely ascribed to the manipulation of the electronic structure of the catalyst surface by Sn doping (Figure 1a). Indeed, density functional theory (DFT) calculations suggest that the introduction of Sn species in CeO_2 facilitates the formation of HCOO*, a key intermediate for formate production, whereas the generation of CO and HER is suppressed.

[a] S. Ning, Z. Guo, Dr. J. Wang, Prof. S. Huang, Prof. X. Kang
School of Environment and Energy
South China University of Technology
Higher Education Mega Center, 382 East Waihuan Road, Guangzhou 510006, China
E-mail: esxkang@scut.edu.cn
[b] Prof. S. Chen
Department of Chemistry and Biochemistry
University of California
1156 High Street, Santa Cruz, CA 95064, USA
E-mail: shaowei@ucsc.edu

Supporting information for this article is available on the WWW under https://doi.org/10.1002/celc.202100445

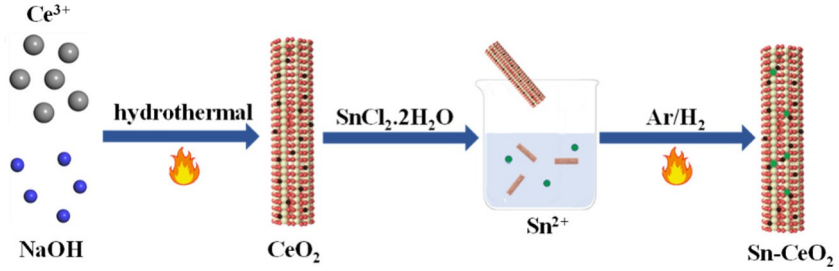

Figure 1. Schematic illustration of the preparation for CeO_2 and Sn-doped CeO_2 nanorods.

2. Results and Discussion

To prepare Sn-doped CeO_2 nanorods, pristine CeO_2 nanorods were first synthesized via a hydrothermal method, and then mixed with a low concentration of $SnCl_2$, followed by thermal annealing in an Ar/H_2 atmosphere, as schematically illustrated in Figure 1a (details in the Supporting Information).

The formation of CeO_2 nanorods was indeed confirmed by transmission electron microscopic (TEM) measurements (Figure 2a), featuring a length of ca. 50 nm and a cross-section diameter of ca. 7.5 nm. With Sn doping increases, the nanorod morphology remained practically unchanged (Figure S1). Figure 2b shows a high-resolution TEM image of Sn-CeO_2-10%, where well-resolved lattice fringes can be observed with a d-spacing of 2.70 Å and 3.14 Å, corresponding to the (200) and (111) crystalline planes of CeO_2 (JSPDS Card# 43-1002), respectively. Furthermore, elemental mapping analysis based on energy-dispersive X-Ray spectroscopy (EDS) exhibits a rather uniform distribution of Ce (red) and Sn (greed) across the sample, suggesting homogeneous doping of Sn into the CeO_2 nanorods (Figure 2c–d).

The crystalline structures of the composites were then characterized by X-ray diffraction (XRD) measurements. As shown in Figure 3a and Figure-S2, Sn-CeO_2-10% nanorods exhibit four diffraction peaks at $2\theta = 28.5°$, 33.1°, 47.5° and 56.4°, which are ascribed to the (111), (200), (220) and (311) crystalline planes of CeO_2 (JSPDS Card# 43-1002), respectively, in good agreement with the HRTEM results (Figure 2). Similar behaviors were observed with other samples in the series. On the basis of the series of high-resolution TEM images taken at different locations of the Sn-CeO_2 nanorods (Figure 2) and the corresponding XRD profile depicted in Figure 3a, CeO_2 is the only crystalline species that can be resolved in the sample, due to a low Sn content.

The elemental composition and valence state of Sn-CeO_2 was then examined by X-ray photoelectron spectroscopy (XPS) measurements.[17] From the high-resolution XPS spectra in Figure 3b and S3, one can see that all the samples exhibited a well-defined Sn 3d doublet at 496.2 and 487.7 eV, due to the $3d_{3/2}$ and $3d_{5/2}$ electrons of Sn (IV) in SnO_2, respectively, while the doublet at 485.2 and 493.6 eV to Sn (0)/Sn(II) $3d_{3/2}$ and $3d_{1/2}$ (low-valence states Sn may arise from thermal reduction under a 10% H_2/Ar atmosphere).[18] In Figure 3c and S4, two core-level signals of the Ce element were observed for all Sn-CeO_2 samples at ca. 900 and 885 eV, corresponding to the Ce $3d_{3/2}$ and $3d_{5/2}$ electrons, respectively.[19] Deconvolution yields five

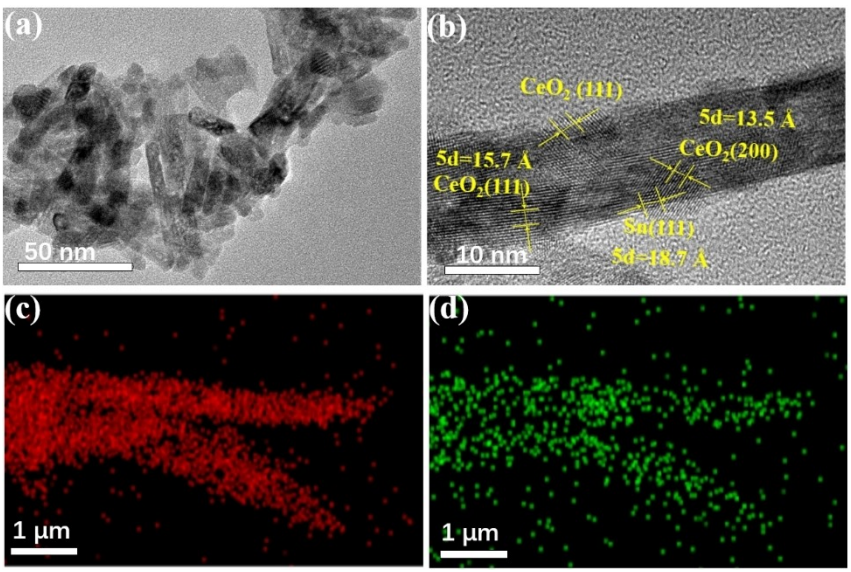

Figure 2. (a) TEM image of CeO_2 nanorods. (b) HRTEM and (c, d) EDS elemental maps of Sn-CeO_2-10% nanorods: Ce (red) and Sn (greed).

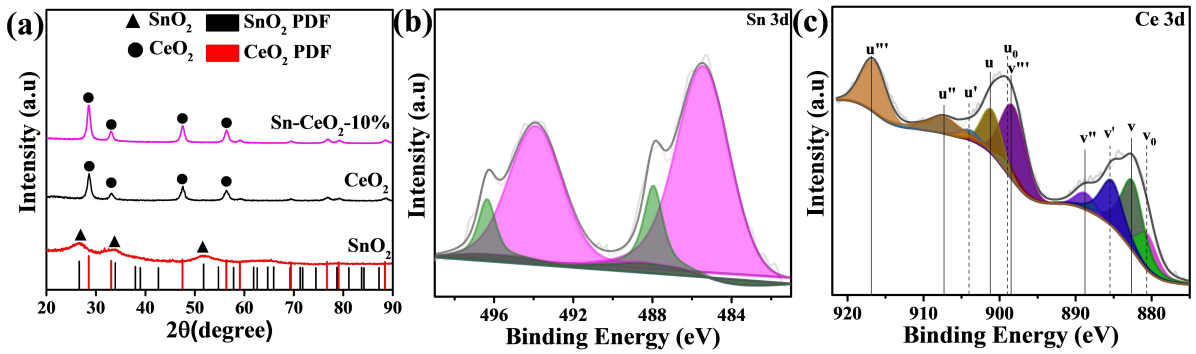

Figure 3. (a) XRD patterns of CeO_2, SnO_2, Sn-CeO_2-10%. (b,c) XPS scans of the (b) Sn 3d and (c) Ce 3d electrons in Sn-CeO_2-10%. Black curves are experimental data and color-shaded peaks are deconvolution fits.

doublets. The pairs of 880.6/898.9 eV and 885.3/903.9 eV most likely arose from Ce^{3+}, indicating the formation of oxygen vacancies on the CeO_2 surface, while those at 882.4/910.0, 888.8/907.3, and 898.2/916.7 eV might be ascribed to Ce^{4+}.[19] Based on the integrated peak areas, the molar ratio of $Ce^{3+}/(Ce^{4+}+Ce^{3+})$ on the sample surface was calculated and listed in Table S1. One can clearly see that the Ce^{3+} content is positively correlated with vacancies. When the ratio of $Ce^{3+}/(Ce^{4+}+Ce^{3+})$ increases and the vacancies increase. On the contrary, the vacancies decrease. When the Sn content is 10%, compared with other catalysts, the value is the lowest 0.182, which indicates that the Sn content doped into CeO_2 vacancies may be the largest. And, with the further increase of Sn content, the ratio of $Ce^{3+}/(Ce^{4+}+Ce^{3+})$ increases, which may be caused by excessive Sn agglomeration.

The charge distributions of CeO_2 and Sn-CeO_2 are shown in Figure S5, where one can see that oxygen vacancies (Vo) are formed around the Sn dopants. This leads to an increase of the Ce valence state compared with the CeO_2, consistent with the XPS results (Figure 3). Note that the formation of Vo facilitated the adsorption of CO_2 molecules, and in conjunction with the adjacent Sn atoms, improved the catalytic activity of CO_2 reduction.[7b] Based on the XPS results, the molar ratio is estimated to be 1:6.3 for Sn^{4+}/Sn^{2+}, and 1:3.5 for Ce^{3+}/Ce^{4+} in Sn-CeO_2-10% (Table 1). When the Sn content exceeds 10%, with an increasing total loading of Sn, the content of low-valence Sn increases accordingly, and inclusions are formed on the CeO_2 surface to agglomerate to reduce the active sites, which leads to a reduced catalytic activity. In addition, one can clearly see that the decrease of Ce^{3+} and Ce^{4+} ratio (from Sn-CeO_2-1% to Sn-CeO_2-10%) can be correlated to the decrease of surface oxygen vacancy concentrations.[20] Meanwhile, an increase of the Sn^{2+} doping level (from Sn-CeO_2-1% to Sn-CeO_2-10%) will lead to a decrease of the $Ce^{3+}/(Ce^{4+}+Ce^{3+}$, Table S1) ratio, as compared to the undoped CeO_2, consistent with the XPS results and theoretical calculation with a low Sn content.

Significantly, the Sn-CeO_2 nanorods exhibited apparent electrocatalytic activity towards CO_2RR, as evaluated in an H-cell filled with CO_2-saturated 0.1 M $NaHCO_3$ solution. Liner sweep voltammetry (LSV) was used to provide an initial, qualitative assessment of the electrocatalytic performance of Sn-CeO_2-10%, undoped CeO_2 and SnO_2, where a sudden increase of voltametric currents was observed in the positive potential sweep from 0 to −1.40 V vs. RHE (Figure 4a), suggesting an apparent CO_2RR catalytic activity. In addition, one can see that the voltametric current density decreases in the order of Sn-CeO_2-10% > SnO_2 > CeO_2 within the potential range. The CO_2RR gas products of CO and H_2 were examined by online gas chromatography (GC), and liquid products were detected by proton nuclear magnetic resonance (NMR) measurements.

The catalyst selectivity was further investigated by electrolysis in a CO_2-saturated 0.1 M $NaHCO_3$ electrolyte. The FE of the products is summarized in Figure 4b–4d and S6. One can see that within the potential range of −0.70 to −1.20 V, CeO_2 mainly catalyzed HER (Figure 4b), with only a trace amount of CO and $HCOO^-$ produced. SnO_2 performed somewhat better towards CO_2RR (Figure 4c), producing a higher selectivity of $HCOO^-$. The best CO_2RR performance was observed with the Sn-CeO_2-10% catalyst (Figure 4d), where electrolysis primarily produced formate, with CO and H_2 being the minor products, and formate production was enhanced at increasingly negative potentials. In fact, the FE of formate was found to increase from 18.80% at −0.70 V to 81.10% at −1.10 V and then decrease slightly to 65% at −1.20 V, markedly better than those of other Sn-CeO_2 samples in the series (Figure S6). For comparison, the FE of formate at −1.10 V was 60% on the SnO_2 electrode (Figure 4c), only 6% for CeO_2 (Figure 4b). That is, Sn-CeO_2-10%

Table 1. Molar ratio of Sn^{4+}/Sn^{2+} and Ce^{3+}/Ce^{4+} of the Sn-CeO_2 samples.

	Sn-CeO_2-1%	Sn-CeO_2-5%	Sn-CeO_2-10%	Sn-CeO_2-15%	Sn-CeO_2-20%
Sn^{4+}/Sn^{2+}	1:7	1:6.5	1:6.3	1:6.6	1:6.8
Ce^{3+}/Ce^{4+}	1:2.5	1:3.2	1:3.5	1:2.9	1:2.7

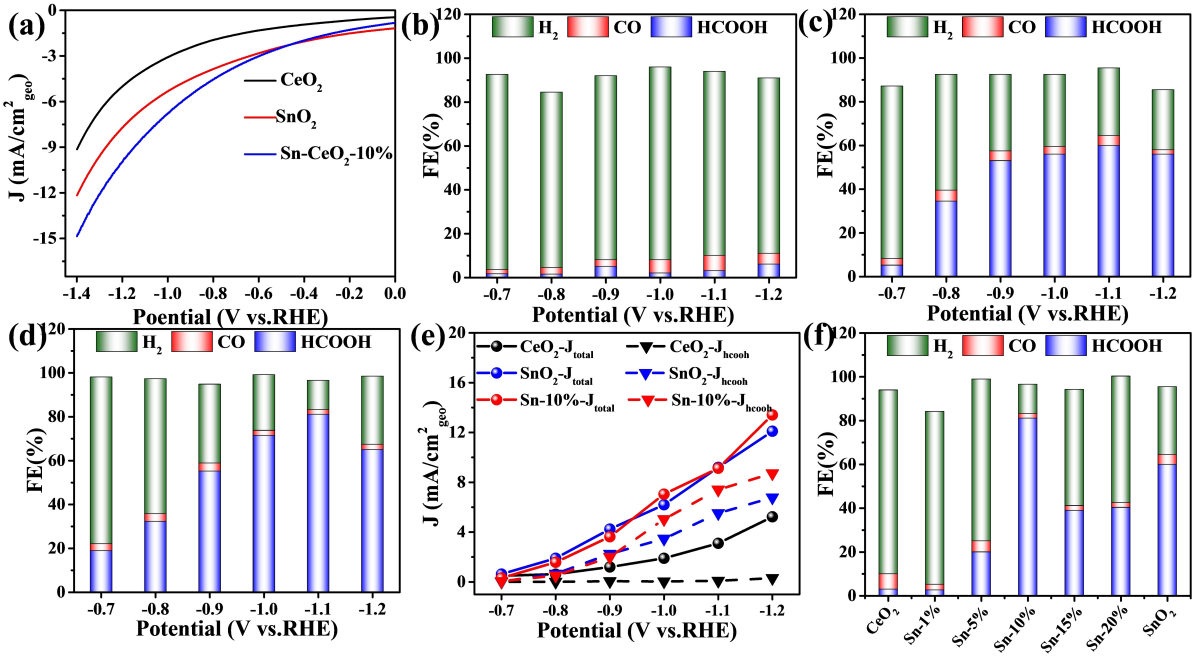

Figure 4. CO_2RR activity of Sn-CeO_2-10%, CeO_2, and SnO_2. (a) LSV curves in CO_2-saturated 0.1 M $NaHCO_3$ electrolyte. FE plots of (b) CeO_2, and (c) SnO_2, (d) Sn-CeO_2-10% at various potentials. (e) Comparison between total current density and formate partial current density. (f) FE comparison of Sn-CeO_2-x%, CeO_2 and SnO_2.

stood out as the best formate production catalyst within the present experimental context.

The total current density (J_{total}) and formate partial current density (J_{hcooh}) of the CeO_2, Sn-CeO_2-10% and SnO_2 are summarized in Figure 4e. Among the three catalysts, Sn-CeO_2-10% demonstrated the highest J_{hcooh}, in agreement with the LSV results (Figure 3a). The enhanced J_{total} can be mainly attributed to the increased amount of Sn^{2+} in the Sn-CeO_2-10% sample, as well as the distinct nature of the catalytic centers. Since J_{total} included the current from HER, J_{hcooh} provided a more accurate account of the CO_2-to-$HCOO^-$ performance. From Figure 4e and S7, one can see that CeO_2 exhibited a J_{hcooh} of only ca. 0.1 mA cm$^{-2}_{geo}$ at −1.10 V, SnO_2 was somewhat better at J_{hcooh} = 5.50 mA cm$^{-2}_{geo}$, and Sn-CeO_2-10% was the highest at ca. 9.13 mA cm$^{-2}_{geo}$, indicating a significant improvement for the intrinsic activity (Figure 4f and S6). This may be ascribed to a higher concentration of Sn active sites in Sn-CeO_2-10% than in other samples, as suggested in XPS measurements (Table 1). Note that Sn aggregation started to occur at high Sn loadings (e.g., Sn-CeO_2-20%), which diminished the number of Sn active sites. In fact, one can see that the double-layer capacitance (Figure S8) of Sn-CeO_2-10% was the highest among the sample series, suggesting a largest electrochemical surface area and ready accessibility of CO_2 to the catalytic active sites. The Sn-CeO_2-10% also exhibited excellent stability (Figure S10). Notably, the current density slightly increases due to the accumulated $HCOO^-$ in the aqueous electrolytic media and the gradual activation of carbon black in the catalyst ink in continuous electrolysis for 23 h.[21] In addition, by comparison with the TEM and XRD of the Sn-CeO_2-10% catalyst before and after CO_2RR (Figures S11–12), no obvious change in the integral structure and morphology, indicating high stability of Sn-CeO_2-10% catalyst during the CO_2RR process.

Sn-doping into CeO_2 lattice could produce oxygen vacancy (V_O) and the synergistic effect of Sn and V_O on the electronic structure o CeO_2 may promote CO_2RR to formate.[7b,22,23] The generation of the first oxygen vacancy (V_O) is spontaneous[24] when a pair of Ce^{4+}-O^{2-} on the CeO_2(111) surface was replaced by a pair of Sn^{2+}-V_O. It was found that the formation energy of the first V_O on the Sn-doped CeO_2(111) surface is lower than two and three oxygen vacancies, as shown in Table S1. As shown in Figure S13a, the HOMO of CeO_2 is mainly composed of the O 2p orbital, and LUMO of the Ce 4f orbital, with a HOMO- LUMO gap of about 2 eV. For Sn-CeO_2, the CeO_2(111) surface was doped with Sn to form a Vo. As shown in Figure S13b, the electrons tend to be located on the Ce 4f orbital occupying the bandgap state, causing the down-shift of the energy level and decrease the bandgap, as compared to undoped CeO_2(111). Figure S9 shows the Nyquist plots of Sn-doping CeO_2 catalysts, which revealed that Sn-CeO_2-10% displayed a lower interfacial charge-transfer resistance (Rct) than other catalysts. The 4-probe method was applied to the electrical conductivity test, and it was found that the electrical conductivity of Sn-CeO_2-10% was significantly higher than that of other catalysts (Table S3). These results indicate that Sn-doped CeO_2 could facilitate electron transfer and also the electrochemical performance of CO_2RR.

Based on the experimental results, two main reaction pathways were considered in the computational analysis. As CO and $HCOO^-$ production involves two-electron and two proton transfers,[25] CO and $HCOO^-$ are formed by the adsorption of

reaction intermediates COOH* and HCOO* on the electrode surface.[18,26] The reaction mechanism is summarized below.

Formic acid mechanism[25b,27]

$$CO_2(g) + e^- + H^+ + * \rightarrow HCOO^* \quad (1\text{-}1)$$

$$HCOO^* + e^- + H^+ \rightarrow HCOOH^* \quad (1\text{-}2)$$

$$HCOOH^* \rightarrow HCOOH\ (aq) + * \quad (1\text{-}3)$$

Carbon monoxide mechanism[27–28]

$$CO_2(g) + e^- + H^+ + * \rightarrow COOH^* \quad (2\text{-}1)$$

$$COOH^* + e^- + H^+ \rightarrow CO^* + H_2O \quad (2\text{-}2)$$

$$CO^* \rightarrow CO\ (g) + * \quad (2\text{-}3)$$

where * represents a surface adsorption site.

To understand the optimized catalytic performance of CO_2RR on Sn-doped CeO_2, the energetics of CO_2RR intermediates to CO and formate were calculated on Sn-CeO_2, CeO_2 and SnO_2 by DFT calculations based on the optimized configurations in Figure S14-16. Note that in CO_2RR, the Tafel slope is a good parameter to the kinetics of the reaction.[29] From Figure S8i, one can see that the measured Tafel slopes plot also reveal that the Tafel slope for formate production on Sn-CeO_2-10% catalyst presents the minimum value. In the CO_2RR process, COOH* and HCOO* are both key intermediates for the formation of HCOOH. From Figure 5a–c, one can see that the formation of HCOO* is a spontaneous exothermic process on Sn-CeO_2, CeO_2 and SnO_2, while the formation of *COOH is endothermic in nature. Also, the energy barrier (ΔG) from HCOO* to HCOOH is observed on Sn-CeO_2(0.34 eV), CeO_2 (0.62 eV) and SnO_2 (0.46 eV), indicating the presence of Vo and doped-Sn favor the formation of HCOOH. Thus, the enhanced activity and selectivity of formate production on Sn-CeO_2(111) ca be attributed to the balanced electrochemical processes between the formation of HCOO* intermediate and the desorption of HCOOH.

Furthermore, according to Mulliken's analysis, there was a charge transfer of 0.13e from Ce to Sn, leading to a change of the electronic structure, consistent with the XPS results. As shown in Figure 5d, the Gibbs free energy of hydrogen (ΔG_H) on Sn-CeO_2, SnO_2 and CeO_2 were calculated to be 1.29, −0.70 and 1.41 eV, respectively. The ΔG_H on CeO_2 is positive, indicating that both HER and formate production are relatively not favored. While ΔG_H on SnO_2 is negative and the adsorption of H on the catalyst is too strong, then the adsorption of H would be competitive to CO_2 and CO_2R might be not favored. Meanwhile, the surface of CeO_2 can accelerate the dissociation of water and increase the coverage of H. Experimentally, we observed that formate production is further promoted on Sn-CeO_2, thus, meaning that the enhanced adsorption of H on Sn-CeO_2 is not strong enough to compete with CO_2 adsorption, but promote the formate formation. These results indicated that HER is suppressed on Sn-CeO_2 which allowed protons to be readily available for formate production, in good agreement with the H_2 FE depicted in Figure 3.

3. Conclusions

In summary, Sn-doped CeO_2 nanorods were prepared via a facile hydrothermal procedure, followed by thermal annealing in Ar/H_2, and exhibited a high performance in selective CO_2 reduction to formate in 0.1 M $NaHCO_3$ solution. This was

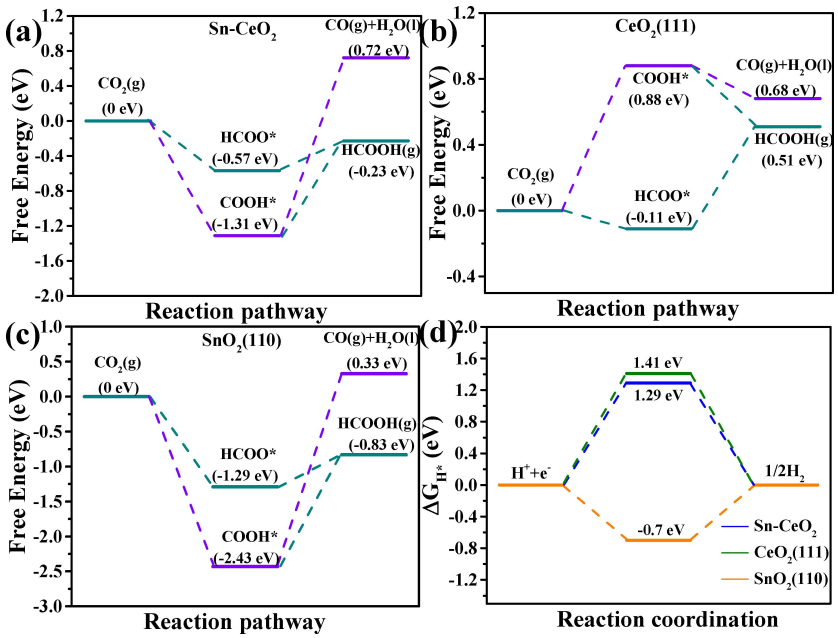

Figure 5. Figure 5. (a) Calculated Free energy diagrams of key CO_2RR intermediates: CO (purple) and HCOOH (cyan) produced on (a) Sn-CeO_2, (b) CeO_2(111), and (c) SnO_2(110). (d) Calculated free-energy diagram of HER on CeO_2 (111), SnO_2(110) and Sn-CeO_2.

attributed to the tuning of surface electronic structures by the synergetic contributions of Sn active sites and oxygen vacancies of CeO_2. Among the series of samples, Sn-CeO_2-10% stood out as the best catalyst, with an FE of 81.10% for formate production and a geometric current density 2.9 times that of CeO_2 at −1.10 V vs. RHE. Theoretical calculations show that the high selectivity was attributed to the Sn doping in ceria that facilitated CO_2 adsorption and decreased the energy barrier to form HCOOH. Results from this study show that deliberate metal doping of CeO_2 can be exploited as an effective strategy in the rational design and engineering of high-performance, low-cost CO_2RR catalysts.

Supplementary Information

Some electrochemical performances, Figure S1–13, Table S1–S2.

Author Information

The authors declare no competing financial interest.

Acknowledgements

This work was supported by the National Natural Science Foundation of China (No. U2032151 and 21773224), National Key R&D Program of China (No. 2018YFB1502600) and the Fundamental Research Funds for Central Universities (SCUT Grant No. 2019ZD22) and Development Program of Guangdong Province (No. 2019B110209002).

Conflict of Interest

The authors declare no conflict of interest.

Keywords: electrochemical CO_2 reduction · Sn-doped CeO_2 · oxygen vacancy · density functional calculations

[1] a) C. Song, *Catal. Today.* **2006**, *115*, 2–32; b) X. Lu, D. Jin, S. Wei, Z. Wang, C. An, W. Guo, *J. Mater. Chem. A.* **2015**, *3*, 12118–12132; c) E. A. Quadrelli, G. Centi, J.-L. Duplan, S. Perathoner, *ChemSusChem.* **2011**, *4*, 1194–1215.
[2] a) K.-P. Yu, W.-Y. Yu, M.-C. Kuo, Y.-C. Liou, S.-H. Chien, *Appl. Catal. B* **2008**, *84*, 112–118; b) F.-W. Chang, M.-S. Kuo, M.-T. Tsay, M.-C. Hsieh, *Appl. Catal. A* **2003**, *247*, 309–320; c) M. Cai, J. Wen, W. Chu, X. Cheng, Z. Li, *J. Nat. Gas Chem.* **2011**, *20*, 318–324; d) I. Omae, *Catal. Today.* **2006**, *115*, 33–52; e) D. Li, N. Ichikuni, S. Shimazu, T. Uematsu, *Appl. Catal. A* **1999**, *180*, 227–235; f) M. Fujiwara, R. Kieffer, H. Ando, Y. Souma, *Appl. Catal. A* **1995**, *121*, 113–124.
[3] a) D. R. Kauffman, J. Thakkar, R. Siva, C. Matranga, P. R. Ohodnicki, C. Zeng, R. Jin, *ACS Appl. Mater. Interfaces.* **2015**, *7*, 15626–15632; b) J. Qiao, Y. Liu, F. Hong, J. Zhang, *Chem. Soc. Rev.* **2014**, *43*, 631–675; c) N. S. Spinner, J. A. Vega, W. E. Mustain, *Catal. Sci. Technol.* **2012**, *2*, 19–28.
[4] a) D. H. Won, H. Shin, J. Koh, J. Chung, H. S. Lee, H. Kim, S. I. Woo, *Angew. Chem. Int. Ed.* **2016**, *55*, 9297–9300; *Angew. Chem.* **2016**, *128*, 9443–9446; b) D. Raciti, K. J. Livi, C. Wang, *Nano Lett.* **2015**, *15*, 6829–6835.
[5] a) C. Guan, D.-D. Zhang, Y. Pan, M. Iguchi, M. J. Ajitha, J. Hu, H. Li, C. Yao, M.-H. Huang, S. Min, J. Zheng, Y. Himeda, H. Kawanami, K.-W. Huang, *Inorg. Chem.* **2017**, *56*, 438–445; b) J.-M. Yan, S.-J. Li, S.-S. Yi, B.-R. Wulan, W.-T. Zheng, Q. Jiang, *Adv. Mater.* **2018**, *30*, 1703038.
[6] B. G. Abraham, K. K. Maniam, A. Kuniyil, R. Chetty, *Fuel Cells.* **2016**, *16*, 656–661.
[7] a) D. Gao, Y. Zhang, Z. Zhou, F. Cai, X. Zhao, W. Huang, Y. Li, J. Zhu, P. Liu, F. Yang, G. Wang, X. Bao, *J. Am. Chem. Soc.* **2017**, *139*, 5652–5655; b) Y. Wang, Z. Chen, P. Han, Y. Du, Z. Gu, X. Xu, G. Zheng, *ACS Catal.* **2018**, *8*, 7113–7119; c) T.-W. Jiang, Y.-W. Zhou, X.-Y. Ma, X. Qin, H. Li, C. Ding, B. Jiang, K. Jiang, W.-B. Cai, *ACS Catal.* **2021**, *11*, 840–848; d) J. Wang, J. Zou, X. Hu, S. Ning, X. Wang, X. Kang, S. Chen, *J. Mater. Chem. A* **2019**, *7*, 27514–27521.
[8] R. J. Gorte, *AIChE J.* **2010**, *56*, 1126–1135.
[9] W. Song, Y. Su, E. J. M. Hensen, *J. Phys. Chem. C* **2015**, *119*, 27505–27511.
[10] Y. Zhao, B. Teng, Z. Yang, Y. Zhao, L. Zhao, M. Luo, *J. Phys. Chem. C* **2011**, *115*, 16461–16466.
[11] B. Jiang, X.-G. Zhang, K. Jiang, D.-Y. Wu, W.-B. Cai, *J. Am. Chem. Soc.* **2018**, *140*, 2880–2889.
[12] a) F. Li, L. Chen, G. P. Knowles, D. R. MacFarlane, J. Zhang, *Angew. Chem. Int. Ed.* **2017**, *56*, 505–509; *Angew. Chem.* **2017**, *129*, 520–524; b) E. Irtem, T. Andreu, A. Parra, M. D. Hernández-Alonso, S. García-Rodríguez, J. M. Riesco-García, G. Penelas-Pérez, J. R. Morante, *J. Mater. Chem. A.* **2016**, *4*, 13582–13588; c) Y. Zhao, J. Liang, C. Wang, J. Ma, G. G. Wallace, *Adv. Energy Mater.* **2018**, *8*, 1702524.
[13] a) N. Han, Y. Wang, H. Yang, J. Deng, J. Wu, Y. Li, Y. Li, *Nat. Commun.* **2018**, *9*, 1320; b) Y. Zhang, F. Li, X. Zhang, T. Williams, C. D. Easton, A. M. Bond, J. Zhang, *J. Mater. Chem. A.* **2018**, *6*, 4714–4720.
[14] Z. B. Hoffman, T. S. Gray, K. B. Moraveck, T. B. Gunnoe, G. Zangari, *ACS Catal.* **2017**, *7*, 5381–5390.
[15] A. Vasileff, C. Xu, L. Ge, Y. Zheng, S.-Z. Qiao, *Chem. Commun.* **2018**, *54*, 13965–13968.
[16] a) M. F. Baruch, J. E. Pander, J. L. White, A. B. Bocarsly, *ACS Catal.* **2015**, *5*, 3148–3156; b) A. Dutta, A. Kuzume, M. Rahaman, S. Vesztergom, P. Broekmann, *ACS Catal.* **2015**, *5*, 7498–7502.
[17] M. Romeo, K. Bak, J. El Fallah, F. Le Normand, L. Hilaire, *Surf. Interface Anal.* **1993**, *20*, 508–512.
[18] Q. Li, J. Fu, W. Zhu, Z. Chen, B. Shen, L. Wu, Z. Xi, T. Wang, G. Lu, J.-j. Zhu, S. Sun, *J. Am. Chem. Soc.* **2017**, *139*, 4290–4293.
[19] H. Dong, L. Zhang, L. Li, W. Deng, C. Hu, Z.-J. Zhao, J. Gong, *Small.* **2019**, *15*, 1900289.
[20] J. Han, J. Meeprasert, P. Maitarad, S. Nammuangruk, L. Shi, D. Zhang, *J. Phys. Chem. C* **2016**, *120*, 1523–1533.
[21] S. Liu, J. Xiao, X. F. Lu, J. Wang, X. Wang, X. W. Lou, *Angew. Chem. Int. Ed.* **2019**, *58*, 8499–8503; *Angew. Chem.* **2019**, *131*, 8587–8591.
[22] C. Guo, S. Wei, S. Zhou, T. Zhang, Z. Wang, S.-P. Ng, X. Lu, C.-M. L. Wu, W. Guo, *ACS Appl. Mater. Interfaces.* **2017**, *9*, 26107–26117.
[23] N. V. Skorodumova, M. Baudin, K. Hermansson, *Phys. Rev. B.* **2004**, *69*, 075401.
[24] J. Paier, C. Penschke, J. Sauer, *Chem. Rev.* **2013**, *113*, 3949–3985.
[25] a) A. Klinkova, P. De Luna, C.-T. Dinh, O. Voznyy, E. M. Larin, E. Kumacheva, E. H. Sargent, *ACS Catal.* **2016**, *6*, 8115–8120; b) J. S. Yoo, R. Christensen, T. Vegge, J. K. Nørskov, F. Studt, *ChemSusChem.* **2016**, *9*, 358–363; c) M. Dunwell, Y. Yan, B. Xu, *ACS Catal.* **2017**, *7*, 5410–5419.
[26] a) J. Wu, R. M. Yadav, M. Liu, P. P. Sharma, C. S. Tiwary, L. Ma, X. Zou, X.-D. Zhou, B. I. Yakobson, J. Lou, P. M. Ajayan, *ACS Nano.* **2015**, *9*, 5364–5371; b) V.-A. Glezakou, L. X. Dang, B. P. McGrail, *J. Phys. Chem. C* **2009**, *113*, 3691–3696.
[27] S. Sen, D. Liu, G. T. R. Palmore, *ACS Catal.* **2014**, *4*, 3091–3095.
[28] H. Huang, H. Jia, Z. Liu, P. Gao, J. Zhao, Z. Luo, J. Yang, J. Zeng, *Angew. Chem. Int. Ed.* **2017**, *56*, 3594–3598; *Angew. Chem.* **2017**, *129*, 3648–3652.
[29] M. Dunwell, W. Luc, Y. Yan, F. Jiao, B. Xu, *ACS Catal.* **2018**, *8*, 8121–8129.

Manuscript received: April 2, 2021
Revised manuscript received: June 5, 2021
Accepted manuscript online: June 28, 2021